

Electronic Supplementary Information (ESI): Mg²⁺ storage and mobility in anatase TiO₂: the role of frustrated coordination

Kit McColl¹ and Furio Corà¹

¹Department of Chemistry, University College London, 20 Gordon Street, London, WC1H 0AJ, United Kingdom

December 18, 2018

Contents

1	Supplementary Methods	2
1.1	Calculations of migration barriers using constrained geometry optimisations	2
1.2	Spin-polarised vs. closed shell calculations	3
2	Supplementary Results	4
2.1	Structural and electronic properties of anatase and Mg at dilute concentrations in the lattice.	4
2.2	Structural properties and energetics of Mg _x TiO ₂	10
2.3	Orderings of Mg in Mg _{0.5} TiO ₂	16
2.4	Structural properties of Mg _{0.5} TiO ₂ configurations.	17
2.5	Structural properties of Mg _{0.5} TiO ₂ phases calculated using a closed-shell configuration.	20

1 Supplementary Methods

1.1 Calculations of migration barriers using constrained geometry optimisations

The activation barriers for ionic migration were determined using constrained geometry optimisations. The first step taken was the optimisation of the initial and final geometries of the ions along the migration pathway. Subsequently, a linear interpolation of the coordinates of the diffusing ion between the two sites was manually calculated leading to a set of images. Initially 9 images were chosen, not including the initial and final geometries. These geometries were relaxed, under the condition that movement of the migrating ion was constrained in the direction of motion. To prevent the entire structure moving with the ion, a single additional ion, chosen as the closest to the migrating ion, had its movement constrained. The energies of the points along the pathway were then calculated relative to the initial or final geometry.

This method allows for a finer interpolation of points along the pathway to be subsequently applied if the position or energy of the activation barrier is not evident. This was implemented for the Mg ion diffusing in the dilute limit ($\text{Mg}_{0.03}\text{TiO}_2$), where clarification of the activation barrier, and precise point at which the Mg ion moved between 5 and 6 fold coordination was required after the first set of 9 images and energies were calculated.

1.2 Spin-polarised vs. closed shell calculations

The results presented in the paper are from spin polarised calculations, under the approximation that the spins of the d^1 electrons on each Ti^{3+} ion are aligned in a ferromagnetic ordering. Whilst this is a reasonable approximation under the conditions of dilute Mg in TiO_2 , this is not necessarily the case at high concentrations of Mg, where the system is expected to become metallic. Representing such metal-insulator transitions is a well-known limitation of DFT; the transition between localised and itinerant electrons for semiconducting metal-oxide systems upon intercalation is challenging to determine and is not well described by any functional.¹ Pure DFT (LDA/GGA) functionals describe metallic states well, but the self-interaction error means that electron localisation is poorly described. Hybrid-exchange functionals describe electron localisation well due to their orbital-dependent cancellation of the self-interaction error, but do not describe metallic behaviour well.

Due to this consideration, we have also examined the structural and energetic properties of the $\text{Mg}_{0.5}\text{TiO}_2$ phases using closed-shell calculations to describe the metallic state. The structural and energetics of the phases from these calculations are reported in Table S4. We find that the same tetragonal to orthorhombic distortions occurs for the metallic state, and the $\text{Mg}_{0.5}\text{TiO}_2$ phase illustrated in Figure 7b (Main text) is the lowest energy, as is the case for the ferromagnetic calculations. The local geometry of the Mg ions in this closed-shell calculated structure is indicated in Figure S16, and the geometry for each Mg ion is similar to that of the ferromagnetic structure (Main text Fig. 8). We also find the same relationship between the relative stability of the $\text{Mg}_{0.5}\text{TiO}_2$ phases and the extent of their a/b distortion as with the ferromagnetic calculations (Fig. S17).

Due to the similarities between the results in the spin-polarised and closed shell calculations, we conclude that the structural distortions occur predominantly as a result of the steric and electrostatic effect of Mg insertion, rather than of electronic localisation. This has also been suggested as the driving force for distortions in the Li_xTiO_2 system.² For this reason, we expect the results for the spin-polarised calculations to give a reliable representation of the behaviour of the system (most importantly the determination of activation barriers) at high concentrations of Mg. The results in the main paper therefore all refer to spin-polarised calculations for consistency.

2 Supplementary Results

2.1 Structural and electronic properties of anatase and Mg at dilute concentrations in the lattice.

Table S1: Calculated structural properties of anatase compared against experimental values.

Method	a (Å)	c (Å)	Vol (Å ³)
Expt.	3.7845	9.5143	136.268
B3LYP	3.7905 (+0.2%)	9.7723 (+2.7%)	140.405 (+3.0%)
B3LYP-D3	3.7663 (-0.5%)	9.5733 (+0.6%)	135.799 (-0.3%)

The electronic density of states are shown in Figure S1. The conduction band is mainly composed of Ti $3d$ states, whose orbital contributions are shown in panel b. The t_{2g} - e_g splitting is evident: the $d_{x^2-y^2}$ and d_{z^2} orbitals are highest in energy. The d_{xz} and d_{yz} orbitals are degenerate, whilst the d_{xy} orbitals in the equatorial plane of the TiO_6 octahedra are slightly split with respect to the d_{xz} and d_{yz} .

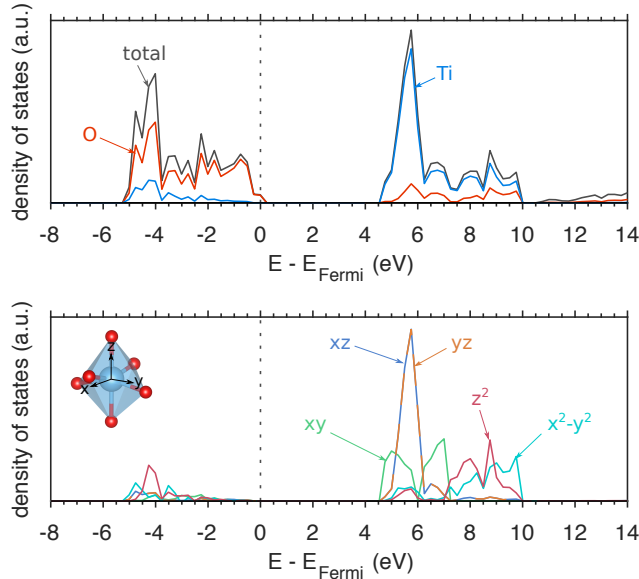


Figure S1: Electronic density of states of anatase TiO_2 and a breakdown of the contributions from the Ti $3d$ orbitals. The d_{xz} and d_{yz} states are degenerate.

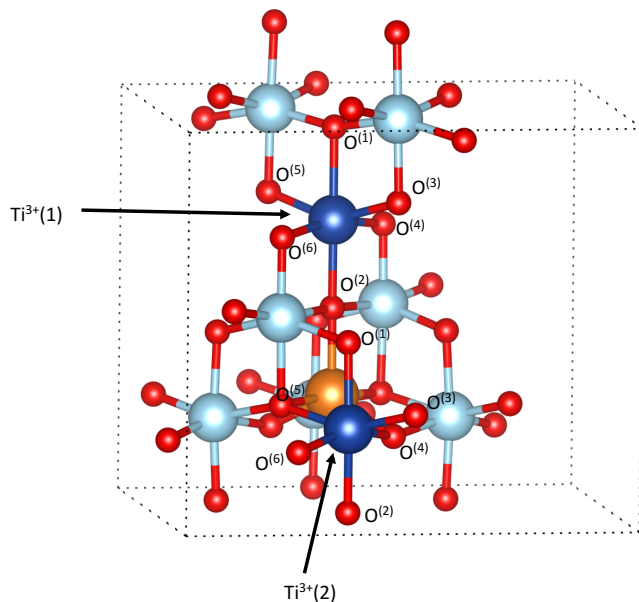


Figure S2: Geometry of Ti^{3+} ions.

Figure S2 shows the geometry of two reduced Ti^{3+} ions upon Mg intercalation in $\text{Mg}_{0.03}\text{TiO}_2$. The two Ti ions are located along the [001] direction and in the same [001] plane relative to Mg. We label them as $\text{Ti}^{3+}(1)$ and $\text{Ti}^{3+}(2)$. The octahedral coordination of the $\text{Ti}^{3+}(1)$ ion is expanded compared to coordination in unmodified TiO_2 , reflecting the increased ionic radius of Ti^{3+} ($r = 0.67 \text{ \AA}$) compared to Ti^{4+} ($r = 0.605 \text{ \AA}$). The Ti-O axial bond towards the Mg ion is lengthened to 2.072 \AA , whilst the opposite axial bond is also stretched to 2.181 \AA . The equatorial Ti-O bonds of $\text{Ti}^{3+}(1)$ are 2.011 \AA , 2.010 \AA , 1.966 \AA and 1.956 \AA . The $\text{Ti}^{3+}(2)$ ion is located on the same [001] plane as the Mg^{2+} , and has axial bond lengths of 2.026 \AA and 1.983 \AA , and equatorial bonds of 2.065 \AA , 2.042 \AA , 1.943 \AA and 1.928 \AA .

Table S2: Ti-O bond lengths in anatase TiO_2 , and the modified Ti^{3+} -O bond lengths upon incorporation of a single Mg ion in $\text{Mg}_{0.03}\text{TiO}_2$.

O ion	Ti^{4+} (anatase) (\AA)	$\text{Ti}^{3+}(1)$ (\AA)	$\text{Ti}^{3+}(2)$ (\AA)
1	1.983	2.181	2.026
2	1.983	2.072	1.983
3	1.927	1.956	1.928
4	1.927	2.010	2.065
5	1.927	1.966	2.042
6	1.927	2.011	1.943

Figure S3a) shows the electronic density of states for the $\text{Mg}_{0.3}\text{TiO}_2$ cell, indicating the contribution from the Ti^{3+} , Ti^{4+} and O^{2-} ions. The introduction of the Mg ion, and the two electrons results in a defect state at ~ 0.8 eV below the conduction band edge, split into two peaks one for each Ti^{3+} ion. Figure S3b) shows the density of states projected onto each Ti $3d$ orbitals for the Ti^{3+} ions. The top panel corresponds to $\text{Ti}^{3+}(2)$. On this Ti^{3+} , the electron is localised in the d_{xy} orbital, which lies across the equatorial plane, pointing towards the Mg^{2+} . The bottom panel shows $\text{Ti}^{3+}(1)$. The electron localised on this ion is in the d_{xz} orbital, which again is the t_{2g} level pointing towards the Mg ion. The spin density isosurfaces are shown in Fig. S4.

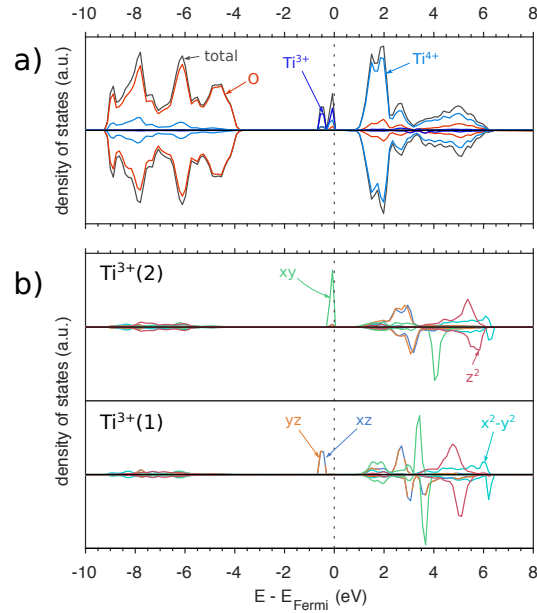


Figure S3: Electronic density of states for the Mg_xTiO_2 structure. The defect state in the bandgap has been multiplied $\times 20$ for clarity. The positive and negative axes represent the spin up and spin down electrons respectively.

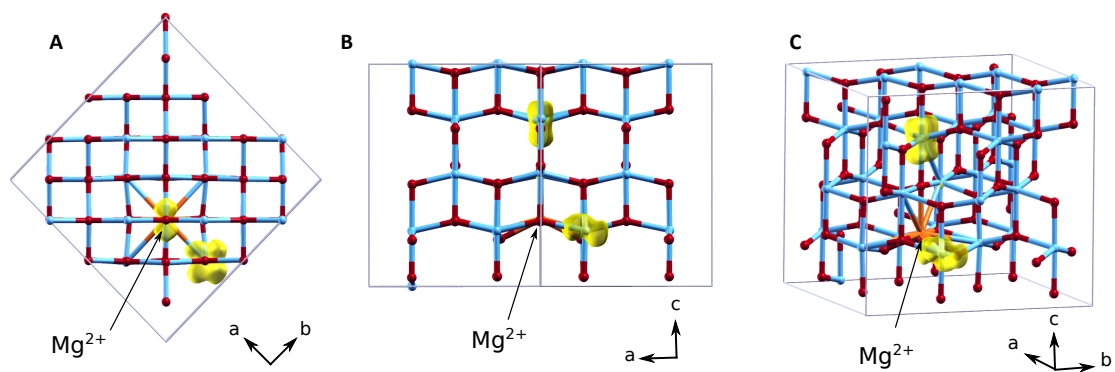


Figure S4: Spin density isosurface for insertion of Mg in anatase at the dilute limit ($\text{MgTi}_{32}\text{O}_{64}$). The isosurface level is set at $0.05 \text{ electrons } \text{\AA}^{-3}$.

Figures S5 and S6 show the geometry of the stationary points identified during the migration profile of the Mg ion in $\text{Mg}_{0.03}\text{TiO}_2$. The migration profile is reported in the main paper in Figure 4B. Figs S5 is the metastable intermediate site obtained at 50% path length, while Fig. S6 is the transition state at 38% path length.

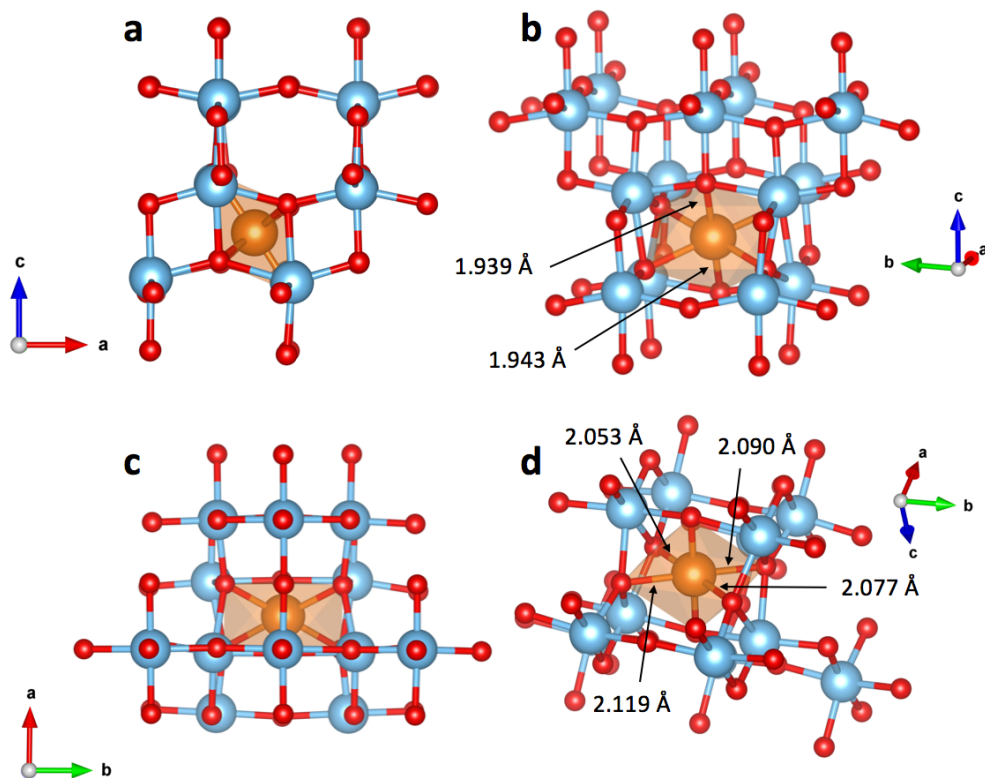


Figure S5: Metastable site

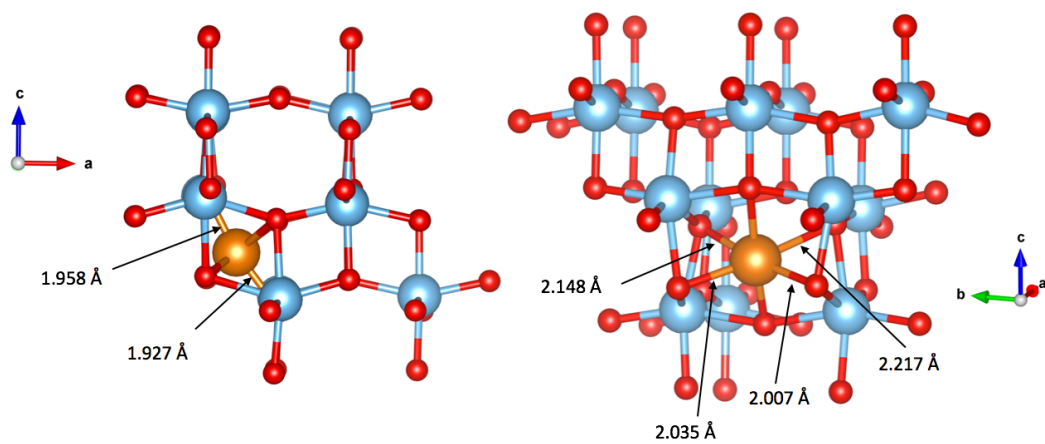


Figure S6: Activated site for Mg

2.2 Structural properties and energetics of Mg_xTiO_2 .

In this section we report the calculated lattice parameters for all the Mg configurations examined in the $(2 \times 1 \times 1)$ anatase cell, as a function of the composition of Mg in Mg_xTiO_2 . This expansion of the unit cell was chosen to give a balance between examining a large number of possible configurations, and keeping the number of calculations low enough to be within computational resources.

Figs. S7-S9 shows the a , b and c lattice parameters. Figs. S10-S12 describe the dependence of stability on the orthorhombic distortion, represented by the ratio of a/b lattice parameters at increasing values of Mg in anatase.

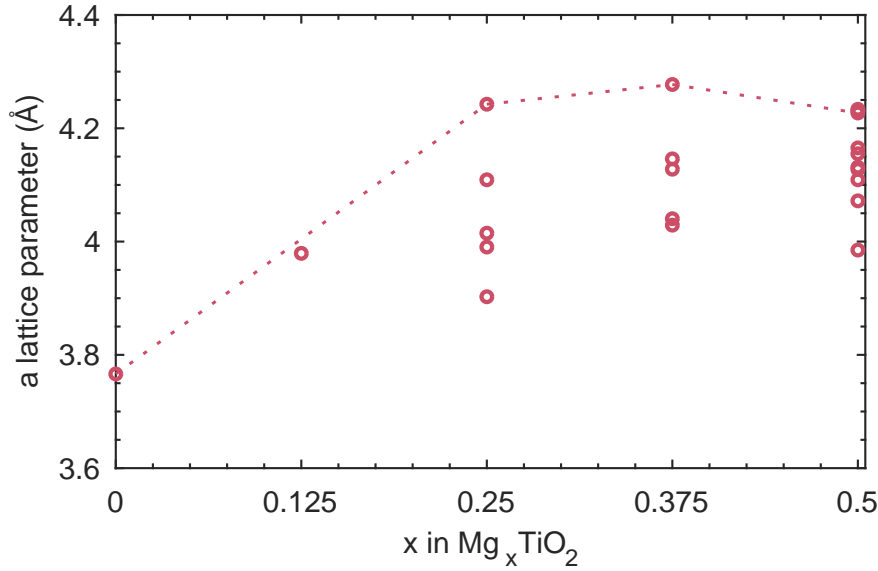


Figure S7: a lattice parameter as a function of Mg concentration. The dotted line links the lowest energy configurations.

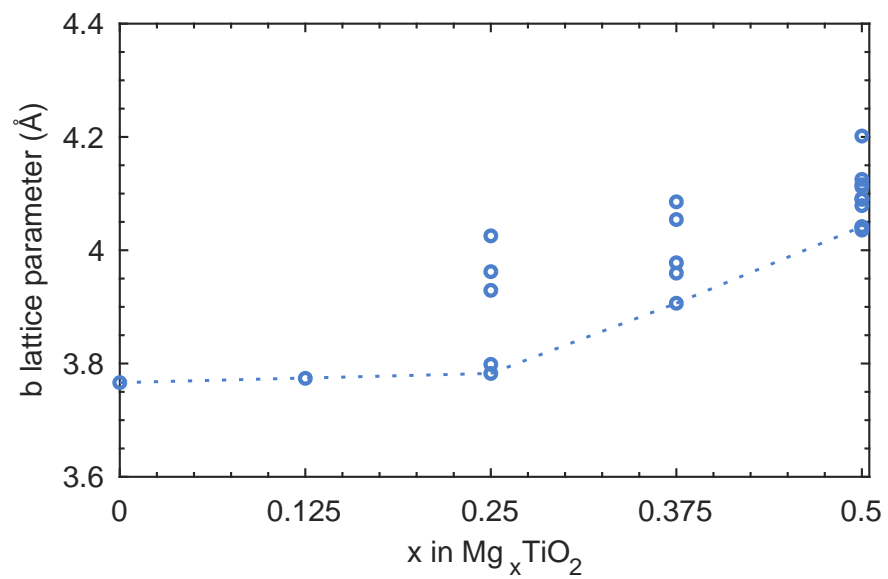


Figure S8: *b* lattice parameter as a function of Mg concentration. The dotted line links the lowest energy configurations.

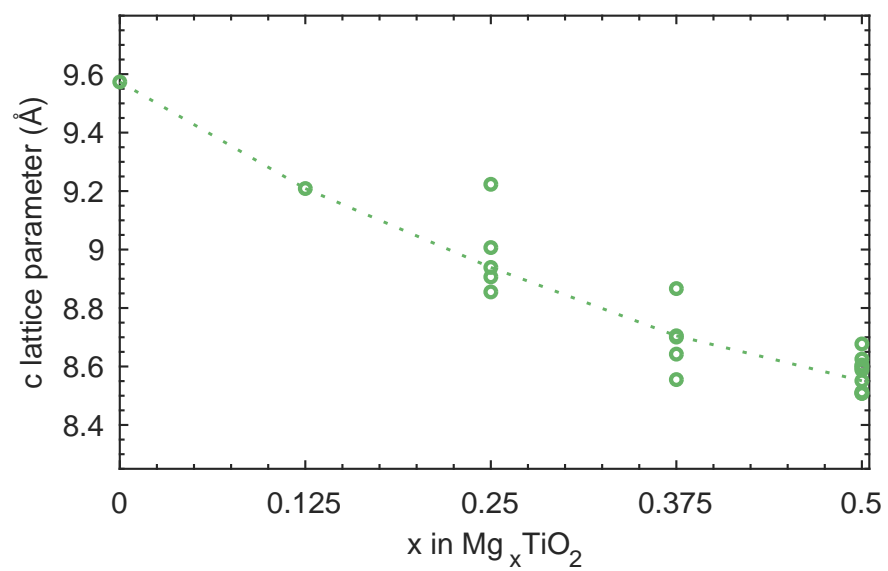


Figure S9: *c* lattice parameter as a function of Mg concentration. The dotted line links the lowest energy configurations.

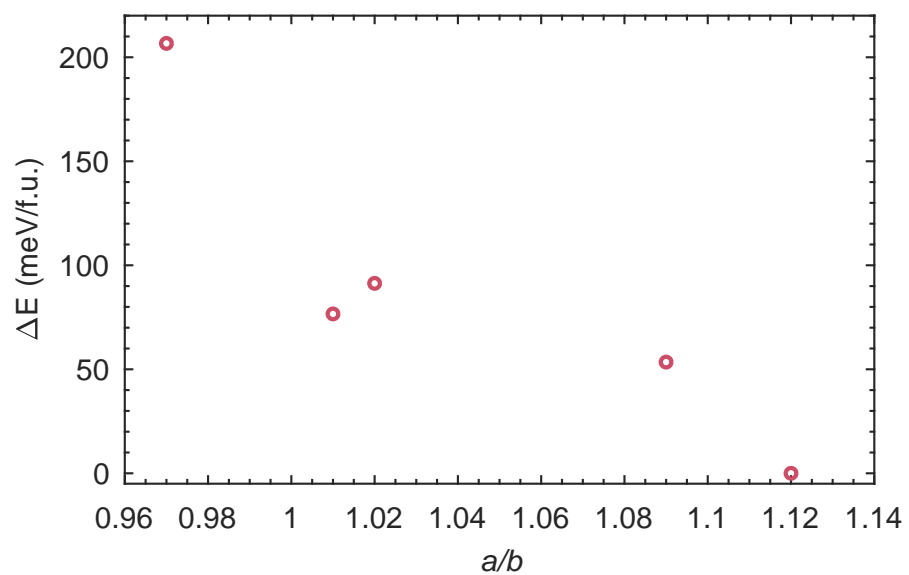


Figure S10: Relative stability of the $\text{Mg}_{0.25}\text{TiO}_2$ configurations examined as a function of the a/b ratio of optimised lattice parameters, representing the orthorhombic distortion of the system.

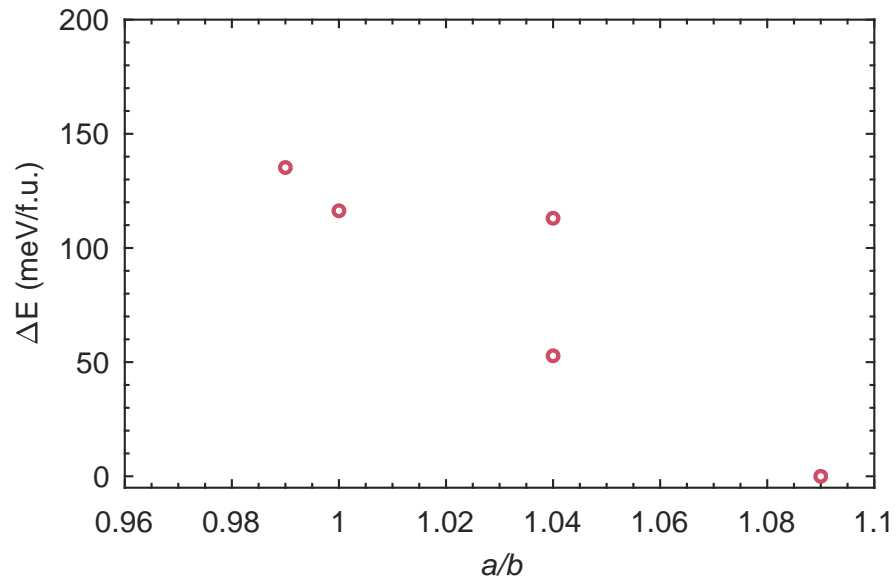


Figure S11: Relative stability of the $\text{Mg}_{0.375}\text{TiO}_2$ configurations examined as a function of the a/b ratio of optimised lattice parameters, representing the orthorhombic distortion of the system.

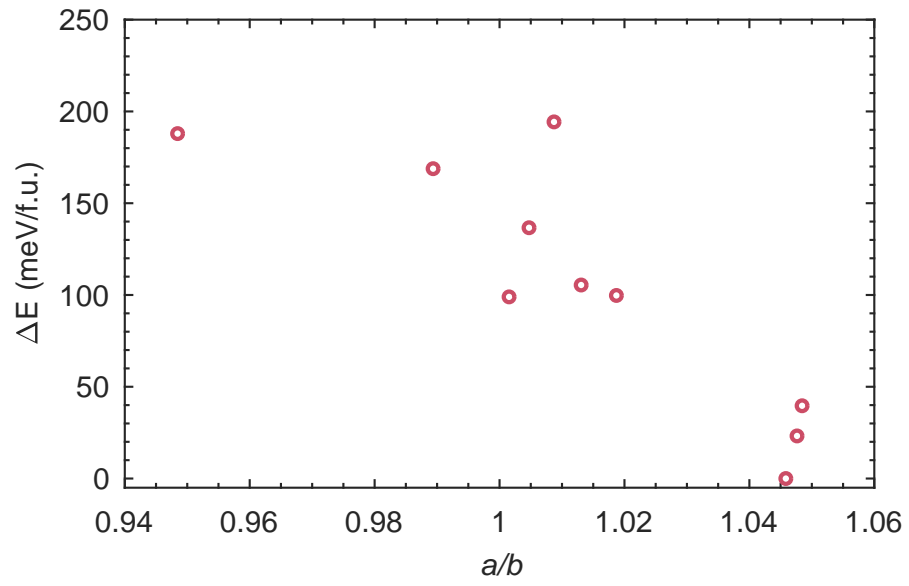


Figure S12: Relative stability of the $\text{Mg}_{0.5}\text{TiO}_2$ configurations examined as a function of the a/b ratio of optimised lattice parameters, representing the orthorhombic distortion of the system.

2.3 Orderings of Mg in $\text{Mg}_{0.5}\text{TiO}_2$.

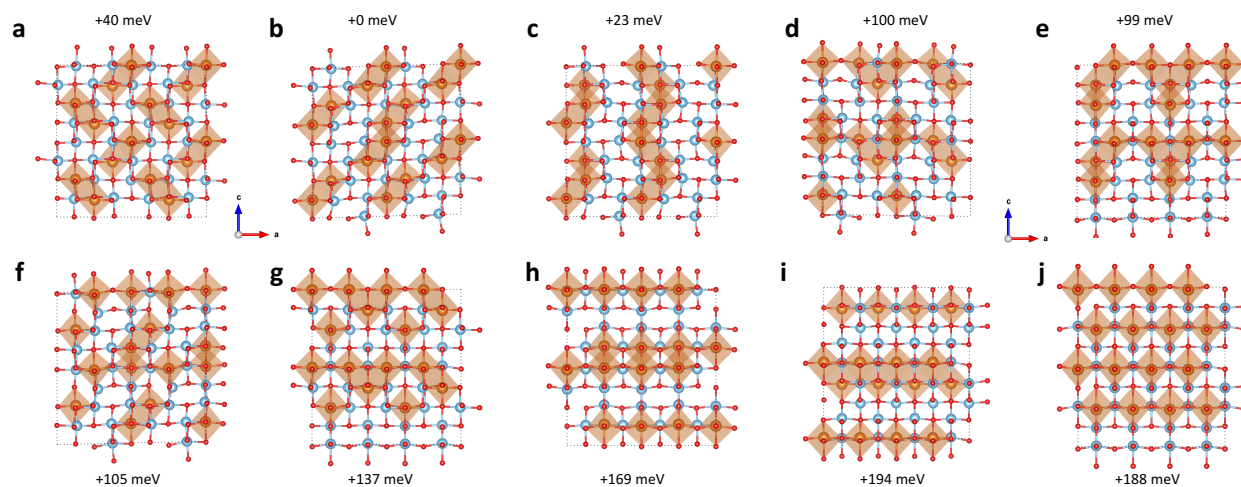


Figure S13: Energetics of Mg ordering in $(2 \times 1 \times 1)$ cells of $\text{Mg}_{0.5}\text{TiO}_2$. Relative energies of the structures are per formula unit (f.u.). Structural properties of configurations a) - j) are reported in Table S3.

2.4 Structural properties of $\text{Mg}_{0.5}\text{TiO}_2$ configurations.

Table S3: Structural and energetic details of different Mg orderings in the $(2 \times 1 \times 1)$ unit cell of $\text{Mg}_{0.5}\text{TiO}_2$. Calculations are spin-polarized, with a ferromagnetic ordering of Ti^{3+} ions. The labels (a-j) correspond to the structures shown in Figure 7 (Main text). Values in brackets give the change compared to the calculated lattice parameters of TiO_2 .

Label	ΔE (meV/f.u.)	Voltage (V)	a (Å)	b (Å)	c (Å)	Vol (Å ³)
a	40	1.91	4.231 (+12.3%)	4.036 (+7.1%)	8.625 (-9.9%)	147.28 (+8.5%)
b	0	1.99	4.227 (+12.2%)	4.042 (+7.3%)	8.551 (-10.7%)	146.09 (+7.6%)
c	23	1.94	4.233 (+12.4%)	4.041 (+7.3%)	8.513 (-11.1%)	145.63 (+7.2%)
d	100	1.79	4.155 (+10.3%)	4.079 (+8.3%)	8.588 (-10.3%)	145.55 (+7.2%)
e	99	1.79	4.131 (+9.7%)	4.125 (+9.5%)	8.508 (-11.1%)	145.00 (+6.8%)
f	105	1.78	4.165 (+10.6%)	4.112 (+9.2%)	8.508 (-11.1%)	145.72 (+7.3%)
g	137	1.71	4.109 (+9.1%)	4.090 (+8.6%)	8.594 (-10.2%)	144.43 (+6.4%)
h	169	1.65	4.072 (+8.1%)	4.116 (+9.3%)	8.605 (-10.1%)	144.21 (+6.2%)
i	194	1.60	4.127 (+9.6%)	4.092 (+8.6%)	8.601 (-10.2%)	145.25 (+7.0%)
j	188	1.61	3.985 (+5.8%)	4.202 (+11.6%)	8.677 (-9.4%)	145.28 (+7.0%)

Fig. S14 shows the three possible inequivalent migration pathways for Mg ions in the most stable phase of $\text{Mg}_{0.5}\text{TiO}_2$.

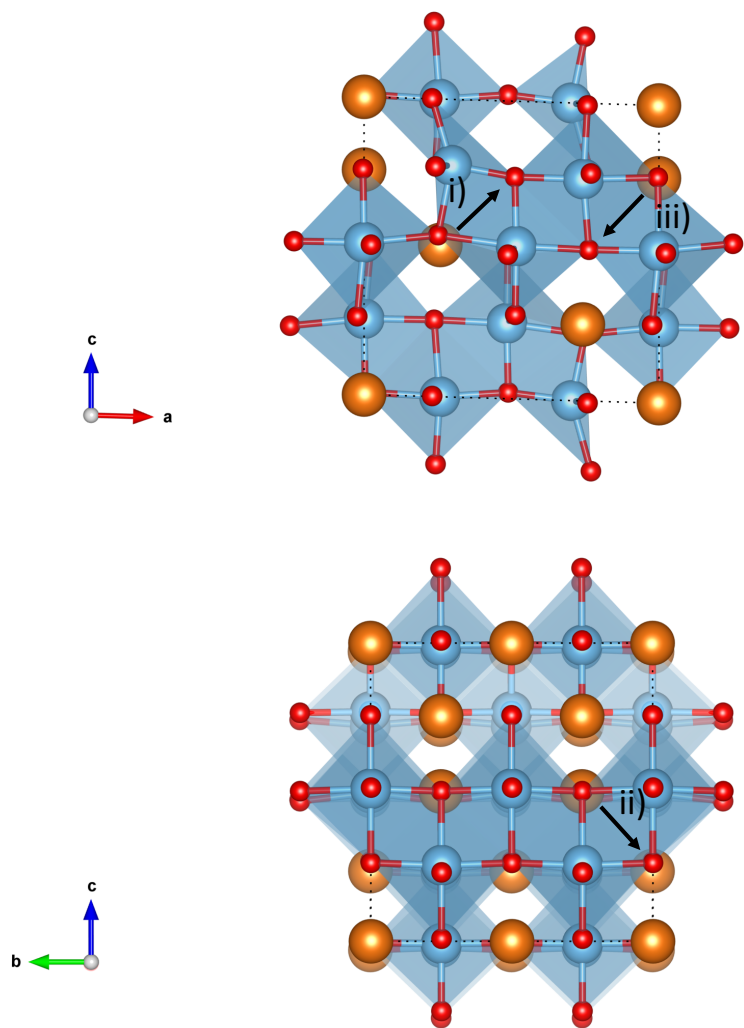


Figure S14: Migration pathways in the lowest energy ordered configuration of $\text{Mg}_{0.5}\text{TiO}_2$. The energetics of the migration profiles along pathways i), ii) and iii) are indicated in the Main Text, Fig. 9.

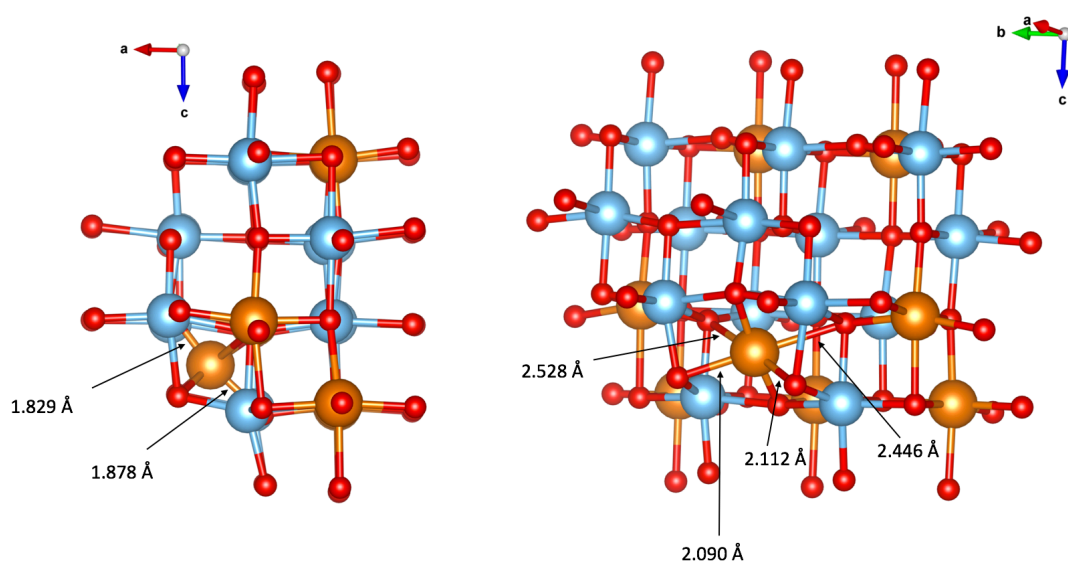


Figure S15: Geometry of the migrating Mg ion in the activated site along pathway i) in the lowest energy ordered structure of $\text{Mg}_{0.5}\text{TiO}_2$

Fig. S15 shows the geometry of the Mg ion in the transition state site along pathway i) in $\text{Mg}_{0.5}\text{TiO}_2$. The Mg^{2+} ion has a distorted octahedral coordination, with non-linear O-Mg-O ‘axial’ bonds. The Mg-O distances along the ‘axial’ bond are shorter (~ 1.83 and ~ 1.88 Å) compared to the equivalent distances at the activated site for Mg diffusion in $\text{Mg}_{0.03}\text{TiO}_2$ (~ 1.94 Å). The Mg^{2+} ion is also pushed slightly towards its initial position along the migration pathway, and thus forms two short and two long equatorial bonds.

2.5 Structural properties of $\text{Mg}_{0.5}\text{TiO}_2$ phases calculated using a closed-shell configuration.

In this section we give a summary of the results obtained using closed shell calculations for the $\text{Mg}_{0.5}\text{TiO}_2$ configurations.

Table S4 summarises the structural properties of each configuration. Fig. S16 shows the coordination of Mg ions in the most stable phase of $\text{Mg}_{0.5}\text{TiO}_2$, and S17 shows the relationship between orthorhombic distortion and relative energy of the configurations.

Table S4: Structural and energetic details of different Mg orderings in a $(2\times 1\times 1)$ unit cell of $\text{Mg}_{0.5}\text{TiO}_2$. Calculations are closed-shell. The labels (a–j) correspond to the structures shown in Figure 7 (Main text). Values in brackets give the change compared to the calculated lattice parameters of TiO_2 .

Label	ΔE (meV/f.u.)	Voltage (V)	a (Å)	b (Å)	c (Å)	Vol (Å ³)
a	153	1.77	4.138 (+9.9%)	3.971 (+5.4%)	8.455 (−11.7%)	138.94 (+2.3%)
b	0	2.08	4.187 (+11.2%)	3.959 (+5.1%)	8.405 (−12.2%)	139.31 (+2.6%)
c	34	2.01	4.168 (+10.7%)	3.962 (+5.2%)	8.475 (−11.5%)	139.96 (+3.1%)
d	252	1.57	4.080 (+8.3%)	4.029 (+7.0%)	8.431 (−11.9%)	138.60 (+2.1%)
e	181	1.72	4.082 (+8.4%)	4.029 (+7.0%)	8.405 (−12.2%)	138.23 (+1.8%)
f	247	1.58	4.086 (+8.5%)	4.047 (+7.5%)	8.446 (−11.8%)	139.68 (+2.9%)
g	314	1.45	4.048 (+7.5%)	4.029 (+7.0%)	8.418 (−12.1%)	137.29 (+1.1%)
h	381	1.32	4.032 (+7.0%)	4.048 (+7.5%)	8.513 (−11.1%)	138.92 (+2.3%)
i	442	1.19	4.122 (+9.4%)	3.994 (+6.0%)	8.670 (−9.4%)	142.72 (+5.1%)
j	447	1.18	3.894 (+3.4%)	4.110 (+9.1%)	8.850 (−7.6%)	141.62 (+4.3%)

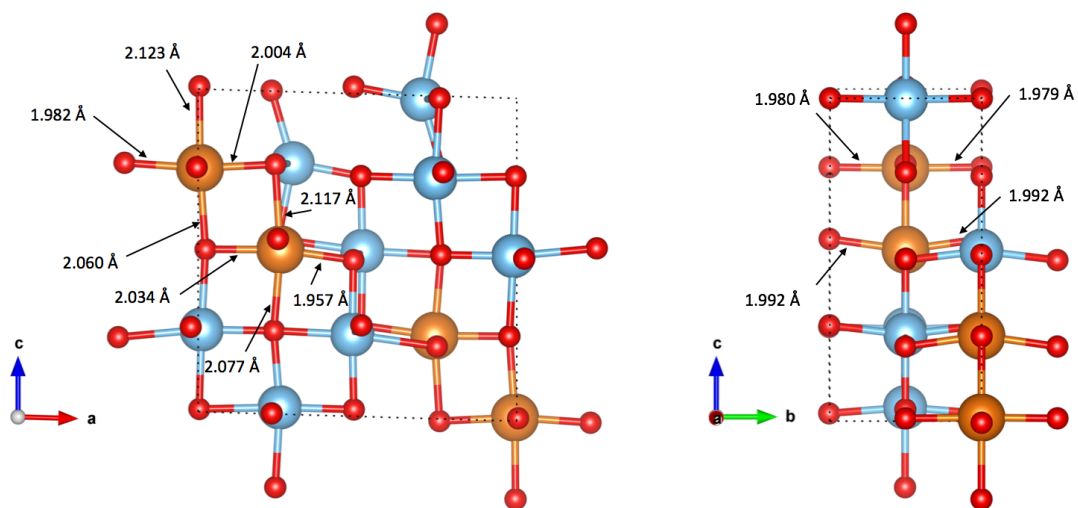


Figure S16: Coordination of Mg ions in the lowest energy configuration of Mg_{0.5}TiO₂ in a closed-shell calculation. Mg-O bond lengths are indicated with arrows pointing to the bonds.

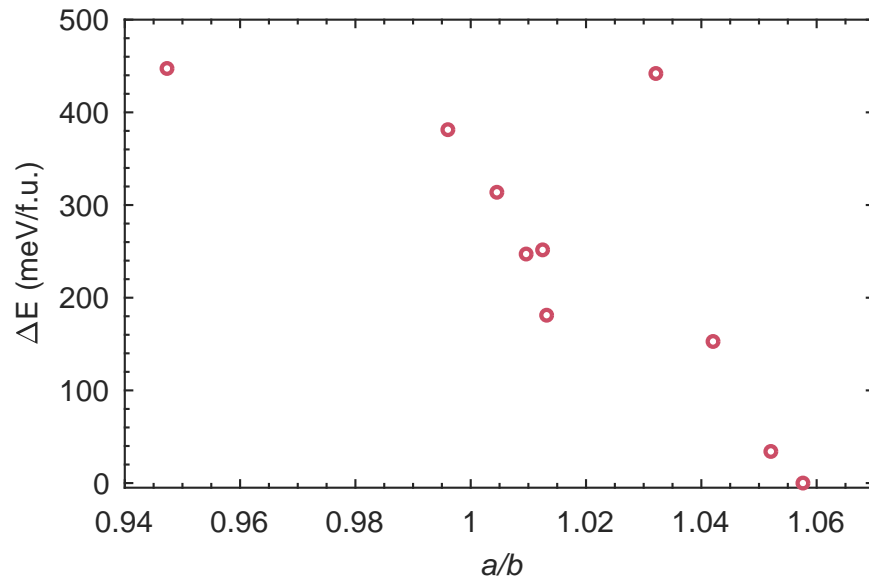


Figure S17: Energetics of the $\text{Mg}_{0.5}\text{TiO}_2$ orderings, as a function of the orthorhombic distortion (a/b), calculated in a closed-shell configuration.

References

- [1] F. Corà, M. Alfredsson, G. Mallia, D. S. Middlemiss, W. C. Mackrodt, R. Dovesi and R. Orlando, *Struct. Bond.*, 2004, **113**, 171–232.
- [2] B. J. Morgan and G. W. Watson, *J. Phys. Chem. Lett.*, 2011, **2**, 1657–1661.